Chemical Engineering Journal 466 (2023) 143112

Contents lists available at ScienceDirect

Chemical Engineering Journal

journal homepage: www.elsevier.com/locate/cej

Conductive nano-gold self-assembled MXene@hemin with high catalytic activity achieved by strong metal-support interactions: A powerful nanozyme for development of electrochemical aptasensor in tuberculosis diagnosis

Yuhan Chen [a], Yue Gu [b], Xiaojuan Yi [c], He Huang [a], Yishi Li [a], Bijun Yang [a], Shuliang Guo [a,*], Lijuan Bai [c,*]

[a] Department of Respiratory and Critical Care Medicine, the First Affiliated Hospital of Chongqing Medical University, Chongqing 400016, PR China
[b] Department of Endocrinology, The First Affiliated Hospital of Chongqing Medical University, Chongqing 400016, PR China
[c] Chongqing Research Center for Pharmaceutical Engineering, College of Pharmacy, Chongqing Medical University, Chongqing 400016, PR China

ARTICLE INFO

Keywords:
Nanozymes
Metal-support interaction
Tuberculosis diagnosis
Electrochemical biosensor

ABSTRACT

Despite multiple advances in tuberculosis (TB), there is still a lack of effective methods available for its diagnosis. To this end, we developed a novel nanozyme-mediated electrochemical aptasensor for TB diagnosis. We showed that hemin decorated with multi-layered MXene enhanced the metal-support interaction with nano-gold via charge transfer, resulting in excellent peroxidase-like activity aside from the highly conductive feature. The K_m value of hemin functionalized MXene decorated with nano-gold (MXene@hemin-Au) was 0.37 mM and 0.23 mM for H_2O_2 and TMB, respectively, which was smaller to that of MXene@hemin (4.01 mM and 0.39 mM) or horseradish peroxidase (3.7 mM and 0.434 mM), indicating its high affinity to both substrates, showing improved stability in harsh conditions and excellent biocompatibility. Given these advantages, an ultrasensitive detection method was established based on a typical sandwich format using a combination of specific *Mycobacterium tuberculosis* (MTB) ESAT-6 antigen aptamers with MXene@hemin-Au as probes for signal amplification and gold nanoparticles supported nitrogen-doped carbon nanotube (N-CNTs-Au) as a sensing platform. It exhibited a wide detection linear for ESAT-6 antigen from 100 fg mL^{-1} to 50 ng mL^{-1}, with limit of detection and limit of quantification of 2.36 fg mL^{-1} and 7.87 fg mL^{-1}, respectively. For its diagnostic application, of note, the proposed method outperformed diagnostic performance for TB in contract to a commercial ELISA method in terms of specificity (100% vs. 20.59%) and area under curve (0.987 vs. 0.596), verifying its great potential in clinical practice.

1. Introduction

Tuberculosis (TB) continues to be a major threat to public health and reliable diagnosis tools play an important role in controlling its burden [1]. TB serological test using *Mycobacterium tuberculosis* (MTB) specific antigen without long-term culture or complex nucleic acid amplification is an appealing way for direct on-site TB diagnosis [2]. Nevertheless, due to the challenging preparation of specific antibodies and their susceptibility to environmental disturbances, their clinical applications have been limited.

Aptamers with superior properties of low cost, easy modification and good stability is considered as a candidate substitute for antibodies and the cooperation with electrical assay exponentially improve the detection performance of diagnostic tools and could provide an alternative way to TB serological tests [3]. For example, Rijiravanich and his colleagues developed a high-performance aptamer-based platform for urinary human albumin electrochemical detection and successfully applied it to urine samples of patients with multiple kidney diseases [4]. Zhang's group used an electrochemical aptasensor to simultaneously detect dual cancer biomarkers, paving the way for accurate prostate cancer diagnosis [5]. Careri's group used aptamers to recognize SARS-CoV-2 spike protein and constructed an electrochemical sensing platform with

* Corresponding authors.
E-mail addresses: guosl999@sina.com (S. Guo), bailj1018@cqmu.edu.cn (L. Bai).

https://doi.org/10.1016/j.cej.2023.143112
Received 23 January 2023; Received in revised form 18 April 2023; Accepted 19 April 2023
Available online 23 April 2023

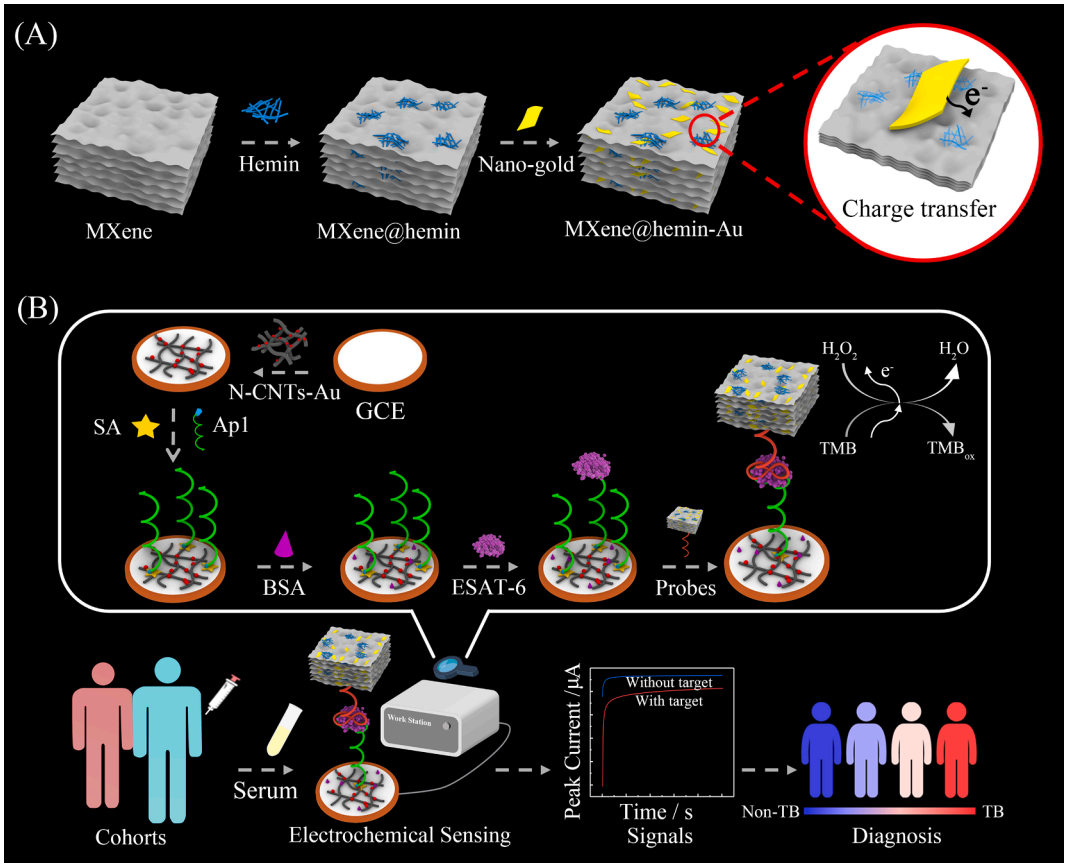

Scheme 1. (A) The process of preparation of nano-gold self-assembled MXene@hemin. (B) The stepwise procedure of the electrochemical aptasensor and its workflow for TB diagnosis. Probes presented MXene@hemin-Au-Ap2.

ultrahigh sensitivity and excellent selectivity [6].

The efficient signal amplification strategy is critical in the development of high-performance electrochemical aptasensors [7]. Nanozyme, a unique nanomaterial that can mimic complexities and functions of natural enzymes, has become a promising amplifier [8]. For example, MXene, a two-dimensional nanomaterial, with large surface area and good conductivity, is more likely to undergo redox reactions than other two-dimension materials due to the existence of low valence Ti and directly reduces metalions the use of additional reducing agents, providing new insights into the design of high-performance nanocatalysts [9]. A recent study reported that MXene-Au nanocomposites can be fine-tuned by adjusting reaction time for enhanced catalytic performances for nitro-compounds [10]. Moreover, the small size and lack of an Au capping agent anchored on the surface of MXene facilitated biomimetic catalysis [11]. Based on these pieces of information, we investigated the biomimetic activity of MXene integration with nanogold and its application for electrochemical assay.

To achieve this, multi-layered MXene was decorated with hemin molecules followed by the assembly of nano-gold via self-reduction routes to create a novel nanozyme (MXene@hemin-Au). Hemin was selected as a modifier on accounts of its unique π-conjugated structure could attach to the surface of two-dimensional nanomaterials via strong noncovalent bond to create a favor interfacial microenvironment, resulting in improved functions [12–14]. Surprisingly, due to the strong metal-support interaction, the obtained nanocatalyst exhibited high conductivity along with excellent peroxidase-like activity and was used to boost the signal intensity in this study.

Herein, we constructed a nanozyme-enabled electrochemical aptasensor using MXene@hemin-Au as a robust signal amplifier for TB diagnosis (Scheme 1). The signal response was immensely amplified owing to the superior charge transfer efficiency and catalytic activity of the MXene@hemin-Au nanozyme. Conductive sensing matrix contributes to the sensitivity improvement of electrochemical assay [15] and nitrogen-doped carbon nanotube combined with AuNPs (N-CNTs-Au) was acted as a sensing platform to accelerate electron transfer and anchor large numbers of aptamers. Using one of MTB specific antigen ESAT-6 as a model target [16], the proposed method was successfully designed in a typical sandwich format and showed excellent diagnostic performance with 90% sensitivity, 100% specificity, and an area under curve (AUC) value of 0.987, outperforming commercial ELISA or other reported tools in TB diagnosis (details in Table 3 and Section 2.9).

2. Experimental

2.1. Study design

This study included a total of 34 TB patients and 20 controls from the First Affiliated Hospital of Chongqing Medical University. Specifically, serum samples of all TB patients were collected according to the WS 288–2017 tuberculosis diagnosis standard [17], with the following patient exclusion criteria: (i) Patients with respiratory failure, heart failure, or other serious diseases, (ii) Patients aged < 18 or > 80 years and, (iii) Pregnant women. For the control group, a total of 20 serum samples were collected from 10 healthy volunteers and 10 volunteers with lung disorders (5 lung cancer cases and 5 chronic obstructive pulmonary disease or COPD cases). The obtained serum samples were kept in clean Eppendorf (EP) tubes marked with corresponding numbers and stored in a refrigerator to be used for commercial ELISA or our proposed detection method. The informed written consent from all participants or next of kin was obtained prior to the research. All experiments were performed in accordance with the Guidelines "Declaration of Helsinki", and approved by the Ethics Committee of the First Affiliated Hospital of

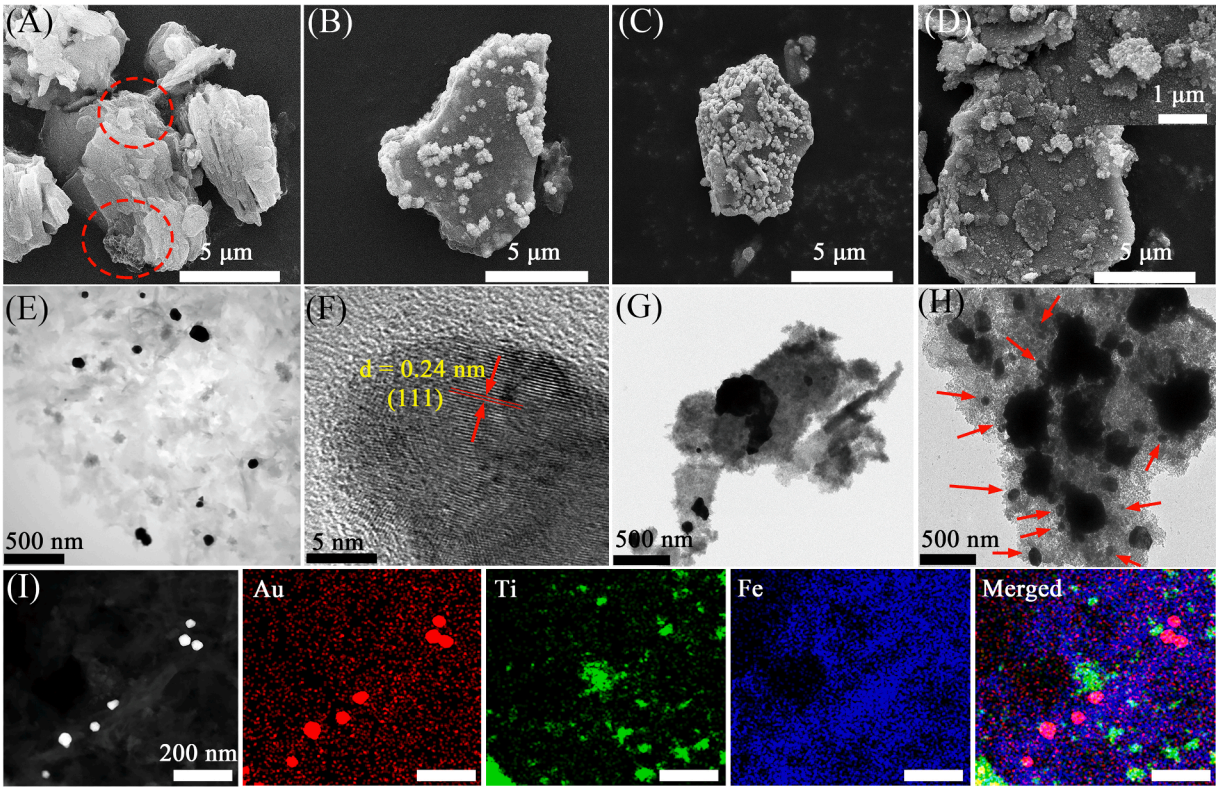

Fig. 1. FE-SEM images of (A) MXene@hemin, (B) MXene@hemin-Au, (C) MXene-Au and (D) MXene@PVP-Au. TEM images of (E) MXene@hemin-Au, (G) MXene-Au and (H) MXene@PVP-Au. (F) HRTEM of nano-gold on the MXene@hemin matrix. (I) HAADF-STEM of MXene@hemin-Au and the corresponding elemental mapping. The inset in Fig. 1 (D) presented a typical structure of huge Au nanocluster in MXene@PVP-Au.

Chongqing Medical University (499PYJJ2021-10).

2.2. Materials and apparatus

2.2.1. Materials

Aptamer 1 (Ap1), aptamer 2 (Ap2) and aptamer 3 (Ap3) of ESAT-6 antigen with the same sequence were designed according to the reference [18] and Ap1 was used to act as capture probes for antigen recognition. Other details of materials are described in the Supplementary Materials.

2.2.2. Apparatus

An electrochemical workstation (CHI660E) was introduced in this study and a three-electrode system was formed using a glassy carbon electrode (GCE) with a diameter of 4 mm as the working electrode, a platinum wire as an auxiliary electrode, and a saturated calomel electrode (SCE) as the reference electrode. Other apparatus included a U1800 spectrophotometer (Shimazu), a Nicolet 6700 FTIR spectrometer (Thermo Nicole), a field emission scanning electron microscope (Thermo Fisher), a high-resolution transmission electron microscope (HRTEM), a transmission electron microscope (Tecnai G2 F20 S-Twin), a powder X-ray diffraction (Bruker D8), an X-ray photoelectron spectroscopy (Thermo Scientific Escalab 250Xi +), and a high-angle annular detector dark-field scanning transmission electron microscopy (Oxford ultim Max).

2.3. Experimental measurements

Electrochemical impedance spectroscopy (EIS) was carried out at a frequency range of 0.1–105 Hz and cyclic voltammetry (CV) was carried out at a voltage range of −0.2–0.6 V (vs. SCE) at a scan rate of 100 mV s^{-1} in a 5 mM $K_3Fe(CN)_6/K_4Fe(CN)_6$ (1:1) solution containing 0.1 M KCl. Amperometric measurements were done at 100 mV in a NaAc-HAc solution (0.2 M, pH = 4) containing 1.3 mM TMB and 10 mM H_2O_2 without stirring. The data were analyzed using three parallel tests, where error bars represent the standard deviation of the mean unless stated otherwise.

2.4. Preparation of MXene-based nanomaterials

A direct mix method was used to prepare hemin-functionalized MXene (MXene@hemin) which was decorated with nano-gold (MXene@hemin-Au) using a self-reaction route. MXene decorated with Au (MXene-Au) and PVP-functionalized MXene decorated with Au (MXene@PVP-Au) were prepared for the control. The stepwise assembly of various MXene-based nanocomposites is illustrated in Fig. S1 and the details are described in the Supplementary Materials.

2.5. Preparation of N-CNTs-Au

The preparation of nitrogen-doped carbon nanotubes decorated with Au nanoparticles (N-CNTs-Au) was done using $NaBH_4$ as a reducing agent, details of which are described in the Supplementary Materials.

2.6. Preparation of MXene-based probes

While MXene@hemin-Au-Ap2 probes were prepared using a mixing method, MXene@hemin-Ap3 probes were prepared by cross-linking, details of which are described in the Supplementary Materials.

2.7. Peroxidase mimicking study

The TMB-H_2O_2 system was used to analyze the biomimetic activity and its details are described in the Supplementary Materials.

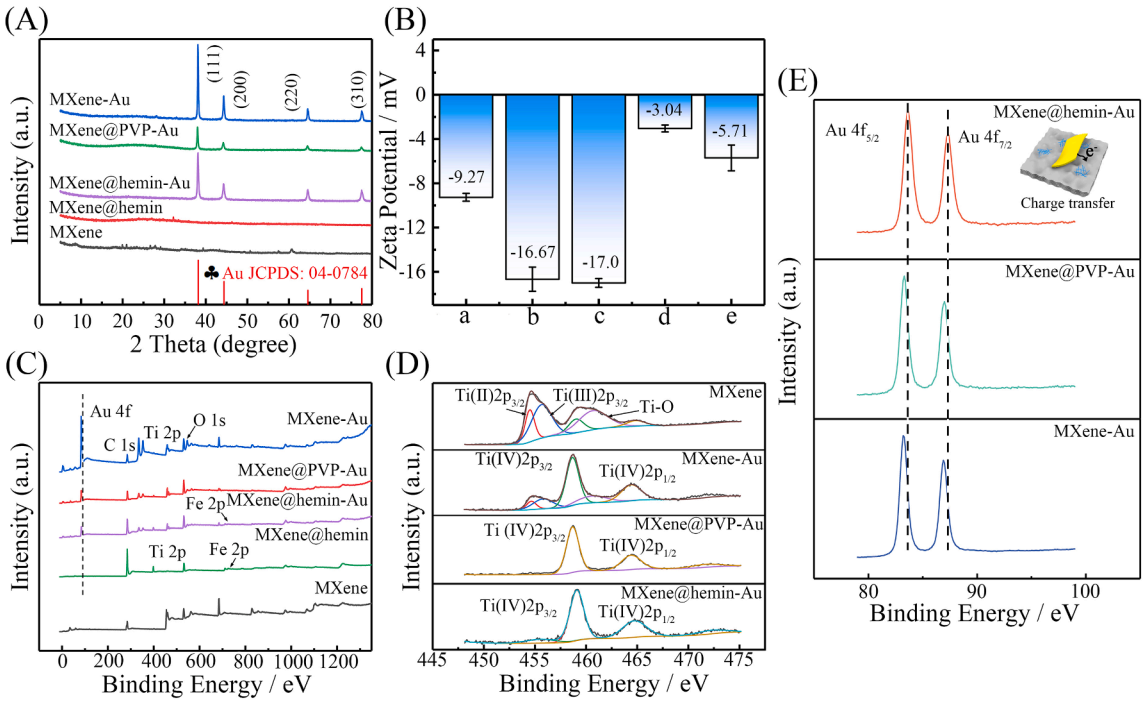

Fig. 2. (A) XRD pattern analysis. (B) Zeta potential analysis (the mean of zeta potential values were marked in corresponding bars): (a) MXene, (b) MXene-Au, (c) MXene@PVP-Au, (d) MXene@hemin, (e) MXene@hemin-Au. (C) Survey XPS data analysis. (D) High resolution Ti 2p analysis. (E) XPS core level spectra of Au 4f analysis.

2.8. In vitro toxicity evaluation

Cytotoxicity and hemolysis tests were performed as described in the Supplementary Materials.

2.9. Fabrication of the nanozyme-mediated electrochemical aptasensor

The details of the steps involved in aptasensor fabrication are presented in the Supplementary Materials.

2.10. Statistical analysis

All the experimental data were arranged in Microsoft Excel software and then further analyzed in Origin Software or Graphpad Prism. These data were expressed as mean ± standard deviation (SD). The data groups were compared using one-way ANOVA and *t*-test to evaluate the correlation between independent variables and obtain the P-value, where $P < 0.05$ was considered to indicate statistically significant. The diagnostic accuracies of our proposed method and commercial ELISA were analyzed using the receiving operating characteristic (ROC) curves. The cut-off points were optimized based on the Youden's index, and diagnostic parameters including sensitivity and specificity were calculated.

3. Results and discussions

3.1. Characterization of MXene-based nanomaterials

Morphologies of the MXene-based nanocomposite series were first determined by field emission scanning electron microscope (FE-SEM) and transmission electron microscopy (TEM). Fig. 1A shows a network (highlighted by a red dotted circle) woven by hemin molecules on the MXene surface, indicating the successful preparation of hemin decorated MXene (MXene@hemin). After self-reduction of $HAuCl_4$ by MXene@hemin, the nano-gold completely dispersed onto the surface of MXene@hemin with a unique flaky morphology (Fig. 1E), while the SEM images showed a popcorn-like structure which was probably due to the partial merging of nano-gold with the scaffold of MXene (Fig. 1B). HRTEM images of MXene@hemin-Au (Fig. 1F) showed a lattice fringe with d-spacing about 0.24 nm corresponding to the (1 1 1) plane of Au, paving further insight into the microstructure of MXene@hemin-Au [19]. Following that, the co-existence of Au, Ti and Fe elements could be observed in Fig. 1I, signifying the successful preparation of MXene@hemin-Au. Moreover, as compared to the SEM images of MXene-Au (Fig. 1C), the morphology and distribution of MXene@hemin-Au nano-gold were more uniform because the small Au nanoclusters of MXene-Au had merged with the large Au bulks, as confirmed by the corresponding TEM images (Fig. 1G). For an in-depth comparison, polyvinylpyrrolidone (PVP) was used to modify MXene as another control and trigger the subsequent self-reduction process. This was because the PVP macromolecular chains can improve the structural stability of MXene [20] as well as serve as a capping agent to facilitate the stability and dispersity of AuNPs [21], resulting in potential changes in their catalytic activities. As observed in Fig. 1D and H, PVP-functionalized MXene (MXene@PVP) mixed with $HAuCl_4$ could produce some spherical Au nanoparticles which tend to form huge nanoclusters. It could be inferred that MXene modifiers could dramatically influence the growth of nano-gold by self-reduction routes, which could explain the difference in their catalyst activities [22].

Additionally, X-ray diffraction (XRD), Zeta potential measurements, and Fourier transform infrared (FTIR) were performed to characterize various MXene-based materials. Fig. 2A shows a comparison of XRD patterns. When hemin was attached to the surface of MXene, the majority of characteristic peaks of MXene disappeared, indicating that the MXene@hemin nanohybrid was successfully formed. In the XRD patterns of MXene-Au, MXene@hemin-Au, and MXene@PVP-Au, four major diffraction peaks assigned to (111), (200), (220), and (311) of face-centered cubic of Au crystalline were observed, indicating that all Au supported on the corresponding MXene-based matrix had a crystalline nature and the (111) plane was the dominant orientation [23]. Fig. 2B shows that, when compared to MXene, different modifications of MXene materials showed varying zeta potentials following the order

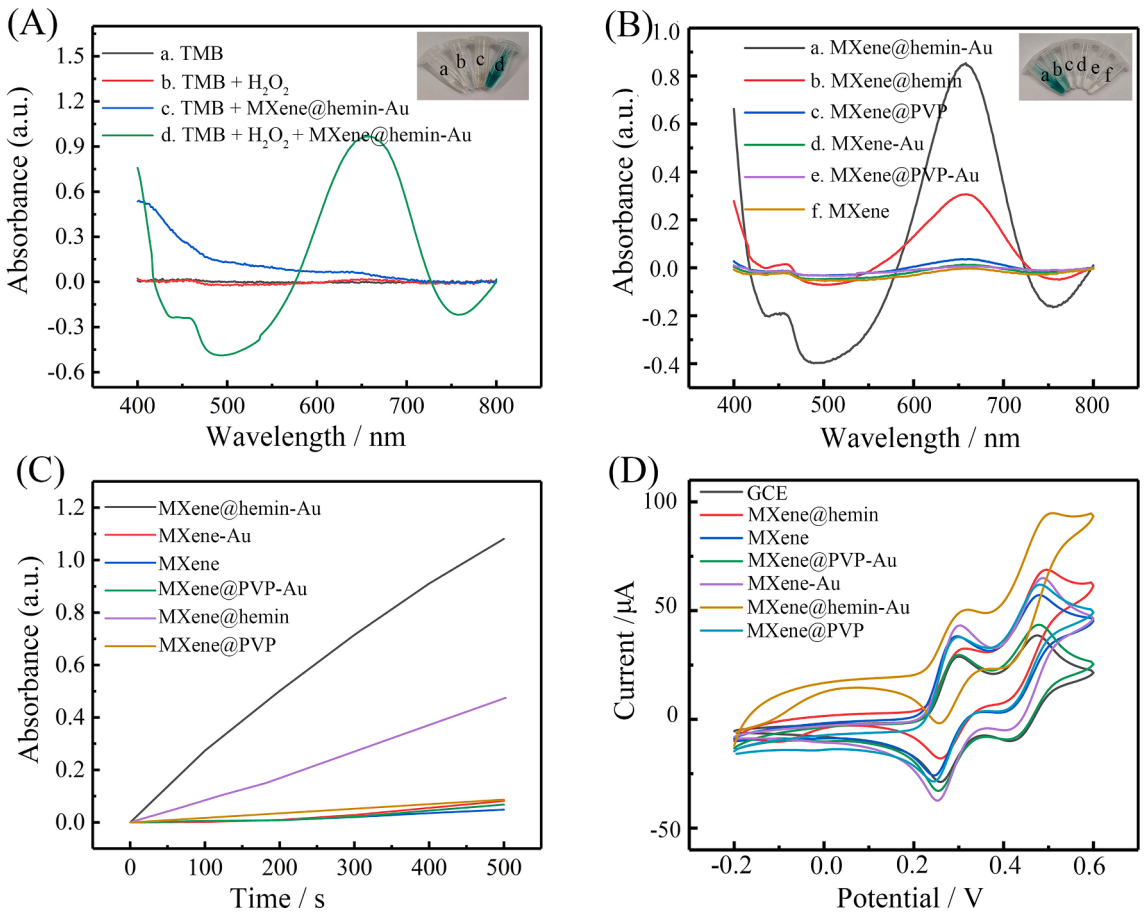

Fig. 3. (A) The absorbance at 652 nm of MXene@hemin-Au in different catalytic systems. (B) Comparison of the catalytic performance of different materials. (C) Time-dependent absorbance changes at 652 nm of different materials. (D) CV responses of different nanomaterials in TMB-H_2O_2 system.

MXene@hemin > MXene@hemin-Au > MXene-Au > MXene@PVP-Au. This indicated the successful fabrication of a series of MXene-based nanomaterials. The interfacial features of MXene@hemin and MXene@PVP were identified using FTIR, details of which are presented in the Supplementary Materials.

An X-ray Photoelectron Spectroscopy (XPS) analysis was performed to investigate the chemical composition and electronic state of various MXene-based nanomaterials. The full scanning spectra showed that the characteristic peaks for Ti 2p, C 1 s, and O 1 s could be observed in all groups, indicating the presence of MXene (Fig. 2C). The XPS scans of MXene-Au and MXene@PVP-Au exhibited an additional peak of Au 4f, suggesting that Au had successfully been attached to MXene or MXene@PVP. Moreover, as compared to MXene, new peaks of Fe 2p and Au 4f could be seen in MXene@hemin-Au, indicating that MXene@hemin-Au had been successfully prepared. Because the element state of Ti was critical to the self-reduction process, we studied the high-resolution spectra of Ti 2p. Compared to the characteristic peaks of delaminated MXene, the initial conversion of Ti (II) and Ti (III) species to the termination of Ti (IV) species was observed in MXene@hemin-Au, MXene-Au, and MXene@PVP-Au, which was consistent with previous studies [10]. In addition, the XPS spectra of the Au 4f core were used to investigate the interaction between nano-gold and MXene-based scaffolds. In MXene@hemin-Au, two peaks located at 83.6 and 87.2 eV, each with a splitting energy of 3.6 eV assigned to Au $4f_{5/2}$ and Au $4f_{7/2}$, indicating the presence of Au (0) in MXene@hemin-Au [24]. The binding energy of Au 4f core level of MXene@hemin-Au showed a visible positive shift as compared to that of MXene@hemin-Au and Mxene-Au, suggesting a stronger interaction between MXene@hemin and Au. This in turn indicated a strong electron transfer from nano-gold to the support [25], where this enhanced metal-support interaction contributed to the stability and activity of the metal nanocatalysts [26,27]. According to the results of the XPS analysis, the estimated Au composition was 13.57%, 2.18%, and 3.69% for MXene-Au, MXene@hemin-Au, and MXene@PVP-Au, respectively, indicating that the spatial distribution of Au could be influenced by various MXene modifications.

3.2. *Peroxidase-like activity study*

Fig. 3A depicts the absorbance of MXene@hemin-Au in different catalytic systems at 652 nm. There were no visible absorbance peaks in MXene@hemin-Au in the presence of TMB but without hydrogen peroxidase (H_2O_2), which suggests that MXene@hemin-Au had negligible oxidase activity. On the contrary, MXene@hemin-Au was able to produce a deep green-colored oxidized TMB solution (TMB_{ox}) and an obvious characteristic peak at 652 nm in the presence of TMB and H_2O_2, indicating an excellent but specific peroxidase-like activity. For MXene@hemin-Au, the self-reduction reaction time was optimized to 60 min for maximum peroxidase-like activity (Fig. S3). Intriguingly, the error bar in Fig. S3 was large, which could be explained by the difficulty in offering a homogeneous reaction environment in a batch reactor [28], indicating synthetic method is an important factor affecting MXene-based self-reactions process apart from the reaction time [10]. Also, the catalytic performances of the nanozymes as well as the natural enzymes were found to be pH and temperature-dependent. In a catalytic reaction, the optimal pH value was 4.5 and the optimal temperature was 37 ℃ (Fig. S4). MXene, MXene-Au, MXene@PVP, and MXene@PVP-Au had no peroxidase-like activity owing to their negligible absorbance values at 652 nm and colorless reaction products (Fig. 3B). In contrast,

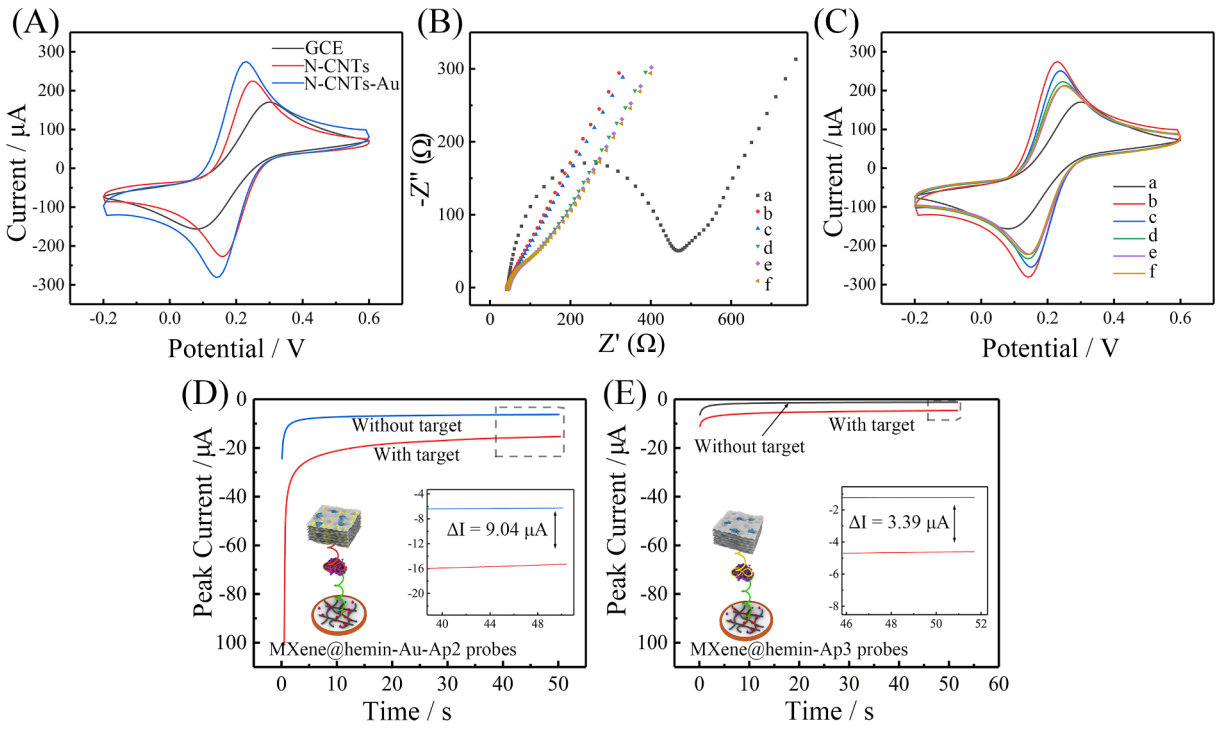

Fig. 4. (A) CVs responses to different modified electrodes. EIS (B) and CVs (C) to step-by-step electrodes construction: (a) bare GCE, (b) N-CNTs-Au modified GCE, (c) streptavidin/N-CNTs-Au modified GCE, (d) Ap1/streptavidin/N-CNTs-Au modified GCE, (e) BSA/Ap1/streptavidin/N-CNTs-Au modified GCE, and (f) BSA/Ap1/streptavidin/N-CNTs-Au modified GCE with ESAT-6 antigen (1 ng mL^{-1}). Detection performance of (D) MXene@hemin-Au-Ap2 probes and (E) MXene@hemin-Ap3 probes.

the peroxidase-like activity of MXene@hemin-Au was significantly high, evident by its time-dependent absorbance at 652 nm. MXene@hemin-Au exhibited the maximum cyclic voltammetry (CV) response in TMB-H_2O_2 systems, which was in agreement with the findings of our UV–vis studies (Fig. 3D).

Furthermore, to confirm if the enhanced biomimetic activity of MXene@hemin-Au was due to the metal-support interaction between MXene@hemin and nano-gold, the absorbance at 652 nm was evaluated for both hemin and hemin@Au. As seen in Fig. S10A, hemin@Au had slightly enhanced peaks at 652 nm when compared to hemin, and the morphology of hemin@Au was bulk block with no observed clear nano-gold structures (Fig. S10B), indicating a very weak interaction between Au and hemin. Therefore, the good peroxidase-like activity of MXene@hemin-Au was more likely due to the charge transfer between nano-gold and MXene-based scaffold.

The superior catalytic performance of MXene@hemin-Au was further validated using enzymatic kinetic constant analysis in addition to other nanozyme characterizations including dispersion, stability, and biocompatibility, the details of which are presented in the Supplementary Materials.

3.3. Characterization and performance verification of N-CNTs-Au

TEM images show small spherical bright spots uniformly surface-dispersed the tubular N-CNTs, indicating the gold nanoparticles had bonded with N-CNTs via Au-N bonds (Fig. S11A). High-angle annular detector dark-field scanning transmission electron microscopy (HAADF STEM) and corresponding element mapping of N-CNTs-Au showed there were Au, C, N and O elements simultaneously (Fig. S11B), verified the successful preparation of such nanohybrid.

CVs were performed to compare the signal responses of different modified electrodes and check if N-CNTs-Au had enhanced the detection performance of the electrochemical assay. N-CNTs-Au-modified electrodes exhibited a higher current response than N-CNTs-modified electrodes or bare GCE (Fig. 4A), indicating good conductivity. Details of electrochemical surface area as an important factor for sensing were presented in the Supplementary Materials.

3.4. Feasibility of the proposed method

CVs and EIS measurements were used to monitor the assembly steps of this method. Electron transfer resistance (R_{et}) was shown as the diameter of the semicircle, where changes could be used to characterize the electrochemical behavior of biosensors. N-CNTs-Au modified electrodes (curve b) showed a much lower R_{et} than bare glass carbon electrodes (GCE, curve a), which could be attributed to enhanced conductivity caused by the synergism of carbon frameworks and noble metals (Fig. 4B). A slightly larger semicircle domain was observed when streptavidin was adsorbed on the modified electrode (curve c). Following that, the association of Ap1 with streptavidin via a strong biotin-avidin system resulted in a slight increase in R_{et} (curve d). The R_{et} further increased after the electrodes were treated with BSA (0.1 wt%) (curve e). Finally, the ESAT-6 antigen (1 ng mL^{-1}) was attached to the modified electrodes via specific aptamer-antigen recognition (curve f), resulting in a slightly larger diameter of the semicircle than curve e. The CV plots showed similar changes in current responses (Fig. 4C).

3.5. Comparison of probe detection performances

We compared the detection performances of MXene@hemin-Au-Ap2 probes and MXene@hemin-Ap3 probes with 1 ng mL^{-1} ESAT-6 antigen in our proposed biosensor. Changes in peak current before and after incubation with or without the target were shown in Fig. 4D and E. The peak current changes of MXene@hemin-Au-Ap2 probes were much higher than that of MXene@hemin-Ap3 (9.04 vs. 3.39 μA). This affirmed the key role of MXene@hemin-Au in improving the detection performance of the proposed method.

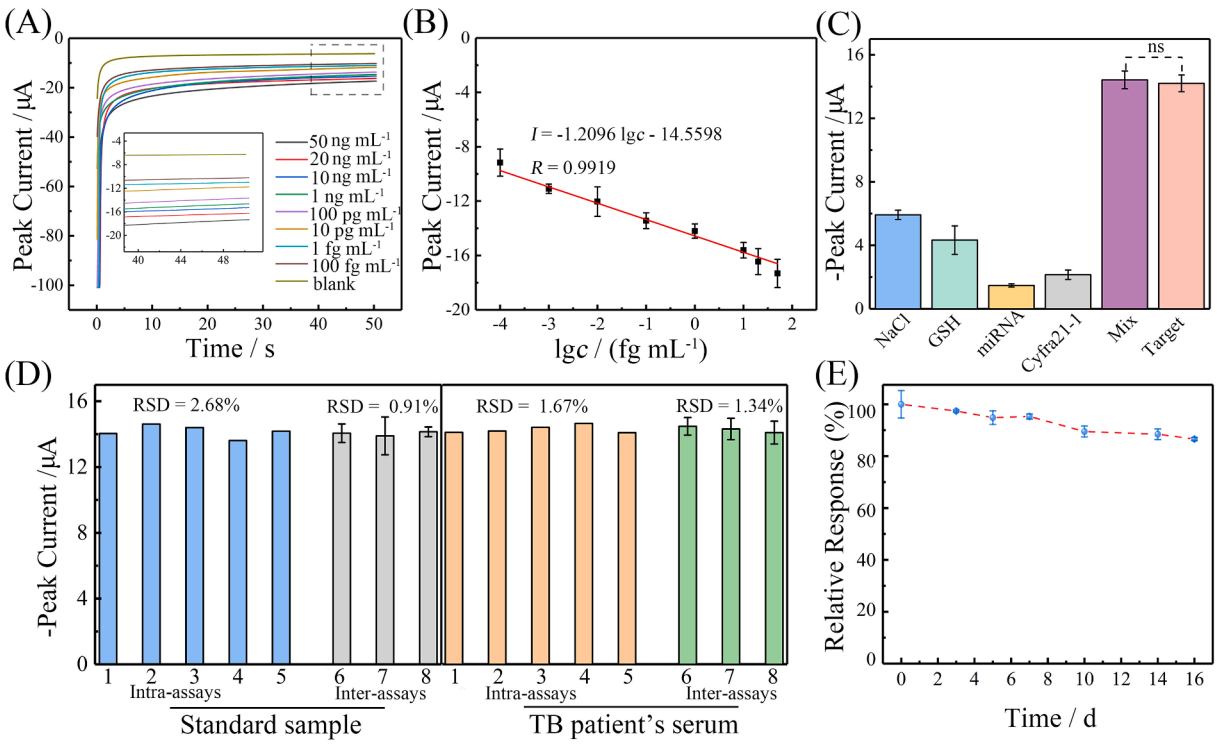

Fig. 5. (A) Amperometric i-t curves of the proposed method toward different concentration of EAST-6 antigen. (B) Linear relation between the amperometric current and the logarithm of ESAT-6 antigen concentration. (C) Selectivity of the proposed method. (D) Reproducibility of the proposed method. (E) Long-term stability of the proposed method. GSH presented glutathione. Error bars represented the SD of three parallel measurements. Data were presented as the mean ± SD (n = 3). The p values are indicated in the charts (ns presented $p > 0.05$).

3.6. Optimization of the electrochemical detection condition

Several important parameters were optimized to maximize the detection performance of the proposed method, details of which are presented in the Supplementary Materials.

3.7. Detection performance of the proposed method

The developed aptasensor was used to detect ESAT-6 antigen via amperometric i-t curves, where amperometric current corresponds to target concentration. The amperometric response increased with the increasing target concentration from 100 fg mL^{-1} to 50 ng mL^{-1} (Fig. 5A). Based on the logarithm of target concentration and amperometric current, the linear regression equation was I = -1.2030 lg$c$ − 14.5598 (Fig. 5B). The limit of detection (LOD) was 2.36 fg mL^{-1}, which was calculated using the equation LOD = 3σ/S, where σ refers to the blank standard deviation and 'S' represents the correction curve slope. The limit of quantification (LOQ) was 7.87 fg mL^{-1}, which was calculated using the equation LOQ = 10σ'/S, where σ' refers to the standard deviation of the lowest concentration [29]. Moreover, the detection performance of our method was consistent with several other methods for TB biomarker detection, confirming its great potential in biomedical application.

Other important factors to be considered while sensor designing include selectivity, reproducibility, and stability. We, therefore, subjected several potential interferences to the proposed method to evaluate its selectivity. As shown in Fig. 5C, there was a negligible signal response in all control groups, where the peak current was lower than blank signal values (the grey dotted line), and the concentration of interference was 10 times higher than the target (1 ng mL^{-1} vs. 100 pg mL^{-1}). For the co-existence of target and interference, the amperometric response of our proposed method approached that of the target group, demonstrating its good selectivity for ESAT-6 antigen. Additionally, to demonstrate its reproducibility, an intra-assay (n = 5) and an inter-assay (n = 3) precision with 1 ng mL^{-1} ESAT-6 antigen and serum from TB patients was probed. The relative standard deviation (RSD) of standard and clinical samples for the intra-assay was 2.68% and 1.67%, respectively, and that for the inter-assay were 0.91% and 1.34%, respectively, demonstrating the excellent reproducibility of the proposed method (Fig. 5D). Finally, the signal intensity after 16 days storage at 4 ℃ remained over 86% of its initial state, demonstrating the acceptable stability of this method (Fig. 5E).

Table 1
Recovery test of the proposed method for ESAT-6 antigen detection in serum samples.

Serum samples	Added ESAT-6 (ng mL^{-1})	Found ESAT-6 (ng mL^{-1})	RSD (%)	Recovery (%)
1	20	19.376	7.2	96.8
2	1	0.942	4.6	94.2
3	10^{-1}	0.108	0.7	108.1
4	10^{-2}	0.092	6.3	92.1
5	10^{-4}	9.98×10^{-5}	5.3	99.7

3.8. Recovery tests of the proposed method

A recovery test of the proposed method was performed using spiked serum samples (Table 1), where we recorded 92.1% to 108.1% recovery and < 10% RSD, suggesting that our method could be used in serum samples to detect the ESAT-6 antigen.

3.9. Potential clinical application analysis

A significantly higher amount of ESAT-6 antigen was detected in the serum of TB cases as compared to the control serum samples (Fig. 6A). Based on Youden's index, the optimal cut-off points and area under

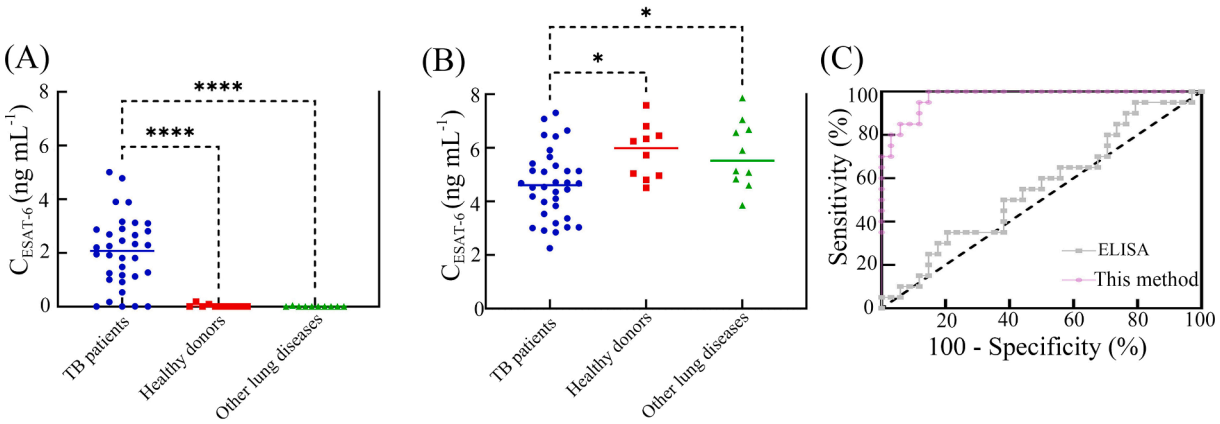

Fig. 6. The clinical application of this method for TB diagnosis. (A) ESAT-6 antigen detection in different groups using this proposed electrochemical aptasensor. (B) ESAT-6 antigen detection in different groups using a commercial ELISA method. (C) ROC curves based on the two methods. Error bars represented the SD of three parallel measurements. Data were presented as the mean ± SD (n = 3). The p values are indicated in the charts (* $p < 0.05$, **** $p < 0.0001$).

Table 2
Comparison of diagnostic performance for TB.

Target	Sample	Method	AUC	Sensitivity	Specificity	Ref.
ManLAM	Serum	ELONA	0.878	83.00%	95.31%	Tang et al., 2016 [30]
MPT-64	Sputum	ELONA	0.9478	91.3%	90%	Sypabekova et al., 2017 [31]
miR–125b	PBMCs	RT-qPCR	0.9413	90%	92.5%	Sun et al., 2021 [32]
cfDNA	Urine	PCR	Not reported	83.7%	100%	Oreskovic et al., 2021 [33]
miR-378	Serum	RT-qPCR	0.849	77.42%	79.37%	Sun et al., 2022 [34]
LAM	EBC	Dot-blot immunoassays	0.997	93.4%	100%	Mosquera-Restreo et al., 2022 [35]
ESAT-6	Serum	ELISA	0.569	95%	20.59%	Commercial kits (in this study)
ESAT-6	Serum	Electrochemical aptasensor	0.987	90%	100%	Our work

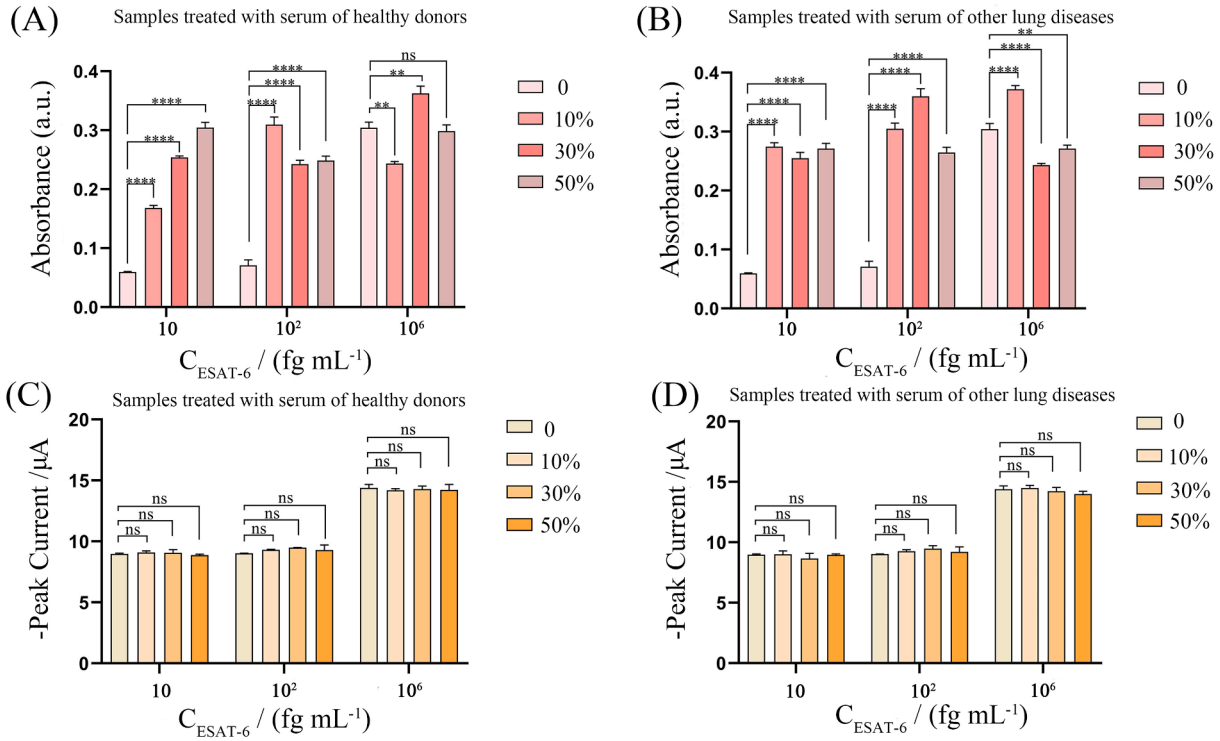

Fig. 7. (A) and (B) The effect of two serum types of varying concentrations on the commercial ELISA method. (C) and (D) The effect of two serum types of varying concentrations on this proposed electrochemical aptasensor. Error bars represented the SD of three parallel measurements. Data were presented as the mean ± SD (n = 3). The p values are indicated in the charts (** $p < 0.01$, **** $p < 0.0001$) and ns presented $p > 0.05$.

curve (AUC) were calculated as 79.2 fg mL^{-1} and 0.987, respectively, with 90% sensitivity and 100% selectivity (Fig. 6C), demonstrating its good diagnostic efficiency. For comparison, a commercial ELISA kit based on antigen–antibody recognition was used. Shown in Fig. S14, the commercial ELISA-based standard curve was established and analyzed by ELISAcalc software using a four-parameter logical model and the correlation coefficient of R^2 was calculated as 0.9360. Therefore, this kit was reliable for subsequent ESAT-6 antigen determination and analysis. The concentration of ESAT-6 antigen in TB cases was found to be similar to that of healthy controls or other lung disorders (Fig. 6B). Apparently, the diagnostic value of commercial ELISA kit was less than satisfactory and the AUC value (0.569) was significantly lower than that of our method (Fig. 6C). We further compared our method with other reported studies in TB diagnosis to point out its importance and advancement (Table 2). Our work showed superior diagnostic value than most of these studies, only slightly inferior to a recent work by Mosquera-Restreo et al. [34] which used exhaled breath condensate (EBC) as samples for LAM (another MTB-specific antigen) determination. We speculate that this difference could be due to the heterogeneity of clinical samples. As a biomarker, the MTB-specific antigen is a promising candidate that can be used to develop diagnostic tools on account of its superior diagnostic value as compared to other biomarkers summarized in Table 2. These findings highlight the potential role of our method for efficient TB diagnosis in clinical practice.

ManLAM, mannose-capped lipoarabinomannan; ELONA, enzyme linked oligonucleotide assay; cfDNA, cell-free DNA; PBMCs, peripheral blood mononuclear cells; RT-qPCR, reverse transcription polymerase chain reaction; PCR, polymerase chain reaction; LAM, lipoarabinomannan; EBC, exhaled breath condensate.

It was obvious that the results of commercial ELISA were counter-intuitive because the ESAT-6 antigen is a specific biomarker for TB which could be ascribed to the matrix effect of serum [36] and the false recognition of polyclonal antibody [37]. To explain this more explicitly, we investigated how the detection performances of our method and commercial ELISA were affected by two serum types of varying concentrations. Shown in Fig. 7A and B, the detection performance of the commercial method was dramatically interfered, especially in the groups with blank or low amount of ESAT-6 antigen. On the contrary, using spiked samples only marginally affected the detection performance of our method (Fig. 7C and D), indicating our method is highly selective and available applied in complex biological samples for clinical detection.

4. Conclusion

In this contribution, a new nanozyme (MXene@hemin-Au) was reported and its application in electrochemical aptasensor for TB diagnosis investigated. The obtained MXene@hemin-Au nanocatalyst possessed could accelerate electron transfer and showed excellent peroxidase-like activity. The excellent biomimetic activity of MXene@hemin-Au could be attributed to (i) the strong metal-support interaction between MXene@hemin and nano-gold contributes to the catalytic performance. (ii) the good dispersity of MXene@hemin-Au resulted in a uniform distribution of nano-gold, exposing its active sites and preventing them from being buried by aggregated scaffolds. It exhibited high stability as well as good biocompatibility. Given these merits, the biosensor built with this new nanozyme for signal amplification showed a wide liner range and low detection limit for ESAT-6 antigen detection. Importantly, the successful application of this method for real-world samples analysis demonstrates its potential in further clinical practice.

Declaration of Competing Interest

The authors declare that they have no known competing financial interests or personal relationships that could have appeared to influence the work reported in this paper.

Data availability

No data was used for the research described in the article.

Acknowledgements

This work is supported by National Natural Science Foundation of China (82072378, 81601856), the National Major Science and Technology Projects of China (2018ZX10302302003), Chongqing Talents: Exceptional Young Talents Project, China (CQYC202005015, cstc2021ycjh-bgzxm0328), Chongqing talents projects-Famous masters and teachers (Shuliang Guo), Ba Yu Scholar Program, China (YS2019020), Program for Youth Innovation in Future Medicine, Chongqing Medical University, China (W0067), Funds for High Level Young Science and Technology Talent Cultivation Plan in Chongqing Medical University, China (2019), Discipline Talent Training Program of College of Pharmacy in Chongqing Medical University, China (YXY2019XSGG4, YXY2021BSH04) and Funds for Young Science and Technology Talent Cultivation Plan of Chongqing City, China (cstc2014kjrc-qnrc00004), Cultivation Foundation of the First Affiliated Hospital of Chongqing Medical University (499PYJJ2021-10). Program for Youth Innovation in Future Medicine, Chongqing Medical University (W0119).

Appendix A. Supplementary data

Supplementary data to this article can be found online at https://doi.org/10.1016/j.cej.2023.143112.

References

[1] World Health Organization, Global tuberculosis report 2021, Switzerland, Geneva, 2021.
[2] Y.K. Yong, H.Y. Tan, A. Saeidi, W.F. Wong, R. Vignesh, V. Velu, R. Eri, M. Larsson, E.M. Shankar, Immune Biomarkers for Diagnosis and Treatment Monitoring of Tuberculosis: Current Developments and Future Prospects, Front. Microbiol. 10 (2019).
[3] A. Villalonga, A.M. Pérez-Calabuig, R. Villalonga, Electrochemical biosensors based on nucleic acid aptamers, Anal. Bioanal. Chem. 412 (1) (2020) 55–72.
[4] L. He, R. Huang, P. Xiao, Y. Liu, L. Jin, H. Liu, S. Li, Y. Deng, Z. Chen, Z. Li, N. He, Current signal amplification strategies in aptamer-based electrochemical biosensor: A review, Chin. Chem. Lett. 32 (5) (2021) 1593–1602.
[5] N. Cheeveewattanagul, C.F. Guajardo Yévenes, S. Bamrungsap, D. Japrung, T. Chalermwatanachai, C. Siriwan, O. Warachit, M. Somasundrum, W. Surareungchai, P. Rijiravanich, Aptamer-functionalised magnetic particles for highly selective detection of urinary albumin in clinical samples of diabetic nephropathy and other kidney tract disease, Anal. Chim. Acta 1154 (2021), 338302.
[6] R. Yan, N. Lu, S. Han, Z. Lu, Y. Xiao, Z. Zhao, M. Zhang, Simultaneous detection of dual biomarkers using hierarchical MoS_2 nanostructuring and nano-signal amplification-based electrochemical aptasensor toward accurate diagnosis of prostate cancer, Biosens. Bioelectron. 197 (2022), 113797.
[7] F. Curti, S. Fortunati, W. Knoll, M. Giannetto, R. Corradini, A. Bertucci, M. Careri, A Folding-Based Electrochemical Aptasensor for the Single-Step Detection of the SARS-CoV-2 Spike Protein, ACS Appl. Mater. Interfaces 14 (17) (2022) 19204–19211.
[8] B. Das, J.L. Franco, N. Logan, P. Balasubramanian, M.I. Kim, C. Cao, Nanozymes in Point-of-Care Diagnosis: An Emerging Futuristic Approach for Biosensing, Nano-micro letters 13 (1) (2021) 193.
[9] A. Sinha, H. Dhanjai, Y. Zhao, X. Huang, J. Lu, R. Chen, Jain, MXene: An emerging material for sensing and biosensing, TrAC Trends Anal. Chem. 105 (2018) 424–435.
[10] K. Li, T. Jiao, R. Xing, G. Zou, J. Zhou, L. Zhang, Q. Peng, Fabrication of tunable hierarchical MXene@AuNPs nanocomposites constructed by self-reduction reactions with enhanced catalytic performances, Sci. China Mater. 61 (5) (2018) 728–736.
[11] S. Wang, W. Chen, A.-L. Liu, L. Hong, H.-H. Deng, X.-H. Lin, Comparison of the Peroxidase-Like Activity of Unmodified, Amino-Modified, and Citrate-Capped Gold Nanoparticles, ChemPhysChem 13 (5) (2012) 1199–1204.
[12] Y. Gu, C. Fan, X. Hao, F. Hu, C. Zhang, H. Yang, C.-M. Li, C. Guo, Oxidase Mimic Graphdiyne for Efficient Superoxide Generation in Wide pH Ranges, Adv. Funct. Mater. 32 (9) (2022) 2110192.
[13] T. Xue, S. Jiang, Y. Qu, Q. Su, R. Cheng, S. Dubin, C.-Y. Chiu, R. Kaner, Y. Huang, X. Duan, Graphene-Supported Hemin as a Highly Active Biomimetic Oxidation Catalyst, Angewandte Chemie International edtion 51 (16) (2012) 3822–3825.

[14] M. Liu, Y. Zhu, D. Jin, L. Li, J. Cheng, Y. Liu, Hemin-Caged Ferritin Acting as a Peroxidase-like Nanozyme for the Selective Detection of Tumor Cells, Inorg. Chem. 60 (19) (2021) 14515–14519.
[15] Z. Wang, Z. Dai, Carbon nanomaterial-based electrochemical biosensors: an overview, Nanoscale 7 (15) (2015) 6420–6431.
[16] L.A.H.v. Pinxteren, P. Ravn, E.M. Agger, J. Pollock, P. Andersen, Diagnosis of Tuberculosis Based on the Two Specific Antigens ESAT-6 and CFP10, Clin. Diagn. Lab. Immunol. 7 (2) (2000) 155–160.
[17] National Health and Family Planning Commission of the People's Republic of China. Diagnosis for pulmonary tuberculosis (WS 288-2017), China, 2017.
[18] X.-L. Tang, Y.-X. Zhou, S.-M. Wu, Q. Pan, B. Xia, X.-L. Zhang, CFP10 and ESAT6 aptamers as effective Mycobacterial antigen diagnostic reagents, J. Infect. 69 (6) (2014) 569–580.
[19] J. Hu, R. Jiang, H. Zhang, Y. Guo, J. Wang, J. Wang, Colloidal porous gold nanoparticles, Nanoscale 10 (39) (2018) 18473–18481.
[20] X. Zhao, L.-Y. Wang, J.-M. Li, L.-M. Peng, C.-Y. Tang, X.-J. Zha, K. Ke, M.-B. Yang, B.-H. Su, W. Yang, Redox-Mediated Artificial Non-Enzymatic Antioxidant MXene Nanoplatforms for Acute Kidney Injury Alleviation, Adv. Sci. 8 (18) (2021) 2101498.
[21] M.V. Bandulasena, G.T. Vladisavljević, O.G. Odunmbaku, B. Benyahia, Continuous synthesis of PVP stabilized biocompatible gold nanoparticles with a controlled size using a 3D glass capillary microfluidic device, Chem. Eng. Sci. 171 (2017) 233–243.
[22] J. Lou-Franco, B. Das, C. Elliott, C. Cao, Gold Nanozymes: From Concept to Biomedical Applications, Nano-micro Lett. 13 (1) (2020) 10.
[23] P.P. Gan, S.H. Ng, Y. Huang, S.F.Y. Li, Green synthesis of gold nanoparticles using palm oil mill effluent (POME): A low-cost and eco-friendly viable approach, Bioresour. Technol. 113 (2012) 132–135.
[24] Y.-H. Chien, C.-C. Huang, S.-W. Wang, C.-S. Yeh, Synthesis of nanoparticles: sunlight formation of gold nanodecahedra for ultra-sensitive lead-ion detection, Green Chem. 13 (5) (2011) 1162–1166.
[25] J. Dong, Q. Fu, Z. Jiang, B. Mei, X. Bao, Carbide-Supported Au Catalysts for Water-Gas Shift Reactions: A New Territory for the Strong Metal-Support Interaction Effect, J. Am. Chem. Soc. 140 (42) (2018) 13808–13816.
[26] S. Cai, Z. Fu, W. Xiao, Y. Xiong, C. Wang, R. Yang, Zero-Dimensional/Two-Dimensional Au_xPd_{100-x} Nanocomposites with Enhanced Nanozyme Catalysis for Sensitive Glucose Detection, ACS Appl. Mater. Interfaces 12 (10) (2020) 11616–11624.
[27] S. Li, Y. Yang, L. Liu, Q. Zhao, Electron transfer-induced catalytic enhancement over bismuth nanoparticles supported by N-doped graphene, Chem. Eng. J. 334 (2018) 1691–1698.
[28] K. Pacławski, B. Streszewski, W. Jaworski, M. Luty-Błocho, K. Fitzner, Gold nanoparticles formation via gold(III) chloride complex ions reduction with glucose in the batch and in the flow microreactor systems, Colloids Surf A Physicochem. Eng. Asp. 413 (2012) 208–215.
[29] W. Wei, M.R. Niñonuevo, A. Sharma, L.M. Danan-Leon, J.A. Leary, A Comprehensive Compositional Analysis of Heparin/Heparan Sulfate-Derived Disaccharides from Human Serum, Anal. Chem. 83 (10) (2011) 3703–3708.
[30] X.-L. Tang, S.-M. Wu, Y. Xie, N. Song, Q. Guan, C. Yuan, X. Zhou, X.-L. Zhang, Generation and application of ssDNA aptamers against glycolipid antigen ManLAM of *Mycobacterium tuberculosis* for TB diagnosis, J. Infect. 72 (5) (2016) 573–586.
[31] M. Sypabekova, A. Bekmurzayeva, R. Wang, Y. Li, C. Nogues, D. Kanayeva, Selection, characterization, and application of DNA aptamers for detection of *Mycobacterium tuberculosis* secreted protein MPT64, Tuberculosis 104 (2017) 70–78.
[32] X. Sun, K. Liu, X. Wang, T. Zhang, X. Li, Y. Zhao, Diagnostic value of microRNA–125b in peripheral blood mononuclear cells for pulmonary tuberculosis, Mol. Med. Rep. 23 (4) (2021) 249.
[33] A. Oreskovic, N. Panpradist, D. Marangu, M.W. Ngwane, Z.P. Magcaba, S. Ngcobo, Z. Ngcobo, D.J. Horne, D.P.K. Wilson, A.E. Shapiro, P.K. Drain, B.R. Lutz, Diagnosing Pulmonary Tuberculosis by Using Sequence-Specific Purification of Urine Cell-Free DNA, J. Clin. Microbiol. 59 (8) (2021) e00074–e00121.
[34] X. Sun, K. Liu, Y. Zhao, T. Zhang, High miRNA-378 expression has high diagnostic values for pulmonary tuberculosis and predicts adverse outcomes, BMC Mol. Cell Biol. 23 (1) (2022) 14.
[35] S.F. Mosquera-Restrepo, S. Zuberogoïtia, L. Gouxette, E. Layre, M. Gilleron, A. Stella, D. Rengel, O. Burlet-Schiltz, A.C. Caro, L.F. Garcia, C. Segura, C.A. Peláez Jaramillo, M. Rojas, J. Nigou, A *Mycobacterium tuberculosis* fingerprint in human breath allows tuberculosis detection, Nat. Commun. 13 (1) (2022) 7751.
[36] J.-F. Masson, Consideration of Sample Matrix Effects and "Biological" Noise in Optimizing the Limit of Detection of Biosensors, ACS Sensors 5 (11) (2020) 3290–3292.
[37] T. Waritani, J. Chang, B. McKinney, K. Terato, An ELISA protocol to improve the accuracy and reliability of serological antibody assays, MethodsX 4 (2017) 153–165.